



FUZZY LOGIC MODELING FOR PROSPECTIVITY MAPPING OF GRANITE-RELATED FRACTURE FILL URANIUM DEPOSITS, ABU HARBA DISTRICT, NORTHEASTERN DESERT, EGYPT

FUZZY LOGICKÉ MODELOVÁNÍ PRO PREDIKTIVNÍ MAPOVÁNÍ URANOVÝCH LOŽISEK VÁZANÝCH NA ZLOMOVÉ ZÓNY V GRANITECH, OBLAST ABU HARBA, SEVEROVÝCHODNÍ POUŠŤ, EGYPT

Islam Azab¹

Abstract

This study utilizes fuzzy logic modeling (FLM) to evaluate the prospectivity mapping for uranium mineralization within the post-collisional A-type granite (PCAG; 630–580 Ma) of the Abu Harba district in the Eastern Desert of Egypt. This district was chosen as a crucial test site because it has three known uranium occurrences and whose geological criteria are deemed the most prospective for uranium mineralization within the Arabian-Nubian Shield (ANS). However, conventional exploration is still challenging there because the terrain is rugged and remote and sub-economic deposit grades. This work presents the first application of the granite-related fracture-fill uranium deposit model within the (ANS). A multi-source geospatial framework was developed, integrating Landsat-8, ASTER, ALOS PALSAR DEM, and airborne gamma-ray datasets to generate evidence layers reflecting key mineralization controls, contextualized with reference to the Schlagintweit deposit analogue in Argentina. The FLM classified prospectivity into five distinct zones, successfully delineating all three known uranium occurrences within high- to very-high-potential areas while excluding 82% of the study area as non-prospective. These results show that FLM is a useful, cost-effective, and efficient tool for uranium exploration in the ANS. They also provide a new, genetically guided framework for future targeting of this type of deposit in the area.

Abstrakt

Tato studie využívá modelování fuzzy logikou (FLM) k vyhodnocení perspektivity a tvorbě prognostické mapy uranové mineralizace v postkolizních granitech typu A (PCAG; stáří 630–580 Ma) v oblasti Abu Harba ve Východní poušti v Egyptě. Tato oblast byla zvolena jako klíčové testovací území, protože se zde nacházejí tři známé výskyty uranové mineralizace a její geologické charakteristiky jsou považovány za nejperspektivnější pro výskyt uranu na Arabsko-núbijském štítu (ANS). Konvenční průzkum je zde však stále náročný díky členitému terénu, odlehlosti a subekonomickým obsahům uranu. Tato práce představuje první aplikaci modelu uranových ložisek vázaných na puklinová rozpukání granitů v rámci ANS. Byl vyvinut více pramenný geoprostorový model, který integrují data z Landsat-8, ASTER, ALOS PALSAR DEM a leteckého gama spektrometrického měření za účelem tvorby vrstev odrážejících klíčové faktory mineralizace, a to s ohledem na analogii s ložiskem Schlagintweit v Argentině. Výsledný FLM klasifikoval perspektivitu do pěti distinktních zón a úspěšně vymezil všechny tři známé výskyty uranu v oblastech s vysokým a velmi vysokým potenciálem, přičemž 82 % území bylo vyloučeno jako neperspektivní. Tyto výsledky dokládají, že FLM představuje užitečný, nákladově efektivní a účinný nástroj pro průzkum uranu na ANS. Zároveň poskytuje nový, geneticky podložený rámec pro budoucí cílení průzkumu tohoto typu ložisek v regionu.

Key words

Fuzzy logic, uranium prospectivity, remote sensing, airborne gamma ray, Eastern Desert, Egypt

Klíčová slova

Fuzzy logika, predikce uranových ložisek, dálkový průzkum Země, aerogama měření, Východní poušť, Egypt

1 Introduction

Uranium exploration in the Eastern Desert (ED) of Egypt has progressed greatly since its inception in the 1950s by the Nuclear Materials Authority (NMA). The ED's basement complex, part of the Neoproterozoic Arabian-Nubian Shield (ANS), exhibits uranium mineralization largely in post-collisional A-type granites (630-580 Ma) produced during East African orogeny tectonism (Eyal et al., 2010). While these granites exhibit uranium promise, deposits are often sub-economic (0.05-0.2% U_3O_8) and fracture-controlled, posing exploration challenges (Cuney & Kyser, 2016; Dawood & El-Naby, 2022). The Abu Harba district presents comparable challenges, since its remote location and substantial height impede conventional investigation. However, the same characteristics make it an excellent research area to utilize novel prospecting approaches.

Recent breakthroughs in remote sensing and GIS-based mineral prospectively modeling (MPM) provide solutions, especially knowledge-driven systems like fuzzy logic that thrive in data-scarce settings (Bonham-Carter, 1994; Porwal et al., 2015). However, although fuzzy logic models have been successfully applied to various deposit types, there is still a significant research gap concerning their tailored use to uranium deposits in the unique geological and climatic conditions of ANS. In the absence of a thorough, multi-source data

integration framework that helps reduce exploration risk in such challenging terrains, previous studies in the area have typically relied on single data sources or qualitative methodologies.

To address this gap, this study develops a tailored FLM designed specifically for uranium prospectivity mapping in the Abu Harba district. This work presents the first application of the granite-related fracture-fill uranium deposit model within the ANS, providing a new genetic framework for exploration. By integrating multi-sensor satellite data (Landsat-8, ASTER, ALOS PALSAR DEM) with airborne gamma-ray surveys, this research establishes a genetically guided, data-driven exploration framework.

The novel contribution of this work is twofold: (1) it provides a rigorously justified, reproducible, and cost-effective methodology for targeting sub-economic, fracture-controlled uranium deposits in remote arid regions by combining publicly available satellite data with geophysical measurements; and (2) it introduces and validates customized fuzzy logic operators and membership functions aligned with the geological characteristics of granite-related fracture-fill uranium systems. The model is validated by its success in identification of all known uranium occurrences in the area and is conceptually supported by the well-documented Schlagintweit deposit in Argentina (Dahlkamp, 2010), which serves as a key analogue for this deposit type.

2 Study area

The study area is located in a highly mountainous sector of the northern Eastern Desert (Fig. 1), which remains geologically under-explored, with only limited prior investigations. The oldest exposed unit consists of metavolcanics (MV), predominantly fine- to very fine-grained metabasalts and meta-andesites, which underwent regional metamorphism up to greenschist facies. These are unconformably overlain by the Dokhan Volcanics (DV), comprising non-metamorphosed andesitic to rhyolitic lava flows interbedded with volcanoclastic deposits. Post-collisional granites dominate the lithology, covering >90% of the area (Fig. 2) and forming major massifs such as Gabal (G.) Abu Harba, G. Urf El Eirr, and G. El-Shehaila. These granites intrude both the MV and DV and exhibit a petrographic gradation from earlier syenogranites (SYG) to later alkali feldspar granites (AFG) Moussa et al. (2008).

The SYG (~40 km² exposure) is coarse-grained, porphyritic, and hematite-stained along fractures, while the AFG (~60 km²) is medium-grained, leucocratic, and hydrothermally altered, with uranium mineralization localized along fault zones. Alteration features include hematitization, kaolinitization, silicification, and Mn-dendrite precipitation. Post-granitic dikes, trending predominantly NE–SW, intrude all units and are classified by cross-cutting relationships into acidic, intermediate, and basic suites.

Uranium occurrences in the AFG are fracture-controlled, dominated by uranyl minerals (β -uranophane, kasolite) (Waheeb, 2016). Three key mineralized zones were identified.

- U.1: A N–S-trending, fracture-intersection-hosted deposit (1 × 0.5 m) with hematitization and silicification.
- U.2: NW-aligned quartz lenses (10 m length) with uranium staining on joint surfaces.
- U.3: A NE–SW fault zone (5 × 0.3 m) along a basaltic dike-granite contact, with pervasive hematitization and kaolinization.

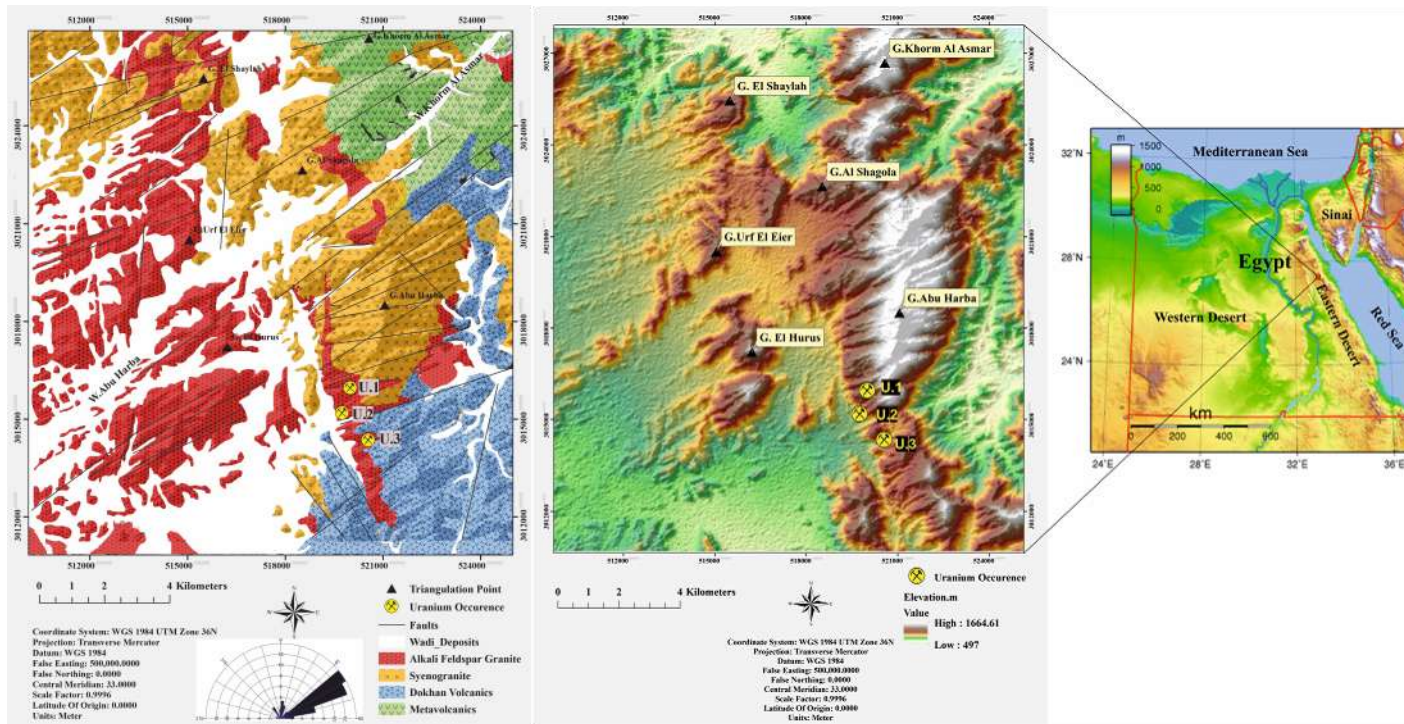


Fig.1. location map, topographic map and geological map of Abu Harba district showing the main rock types, uranium occurrences and main faults with rose diagram showing the main trends. Geological map modified after [Moussa et al. \(2008\)](#)

3 Materials and methods

3.1 Multispectral data

Both L8 and cloud-free ASTER Level 1T (AST_L1T) scenes covering the study area were acquired from USGS Earth Explorer on 20 May 2023 (<https://earthexplorer.usgs.gov>). The raw VNIR and SWIR datasets underwent preprocessing, including radiometric calibration, atmospheric correction (FLAASH), and minimum noise fraction (MNF) using ENVI 5.3 (L3Harris Geospatial), following Javhar et al. (2018) to convert DN to reflectance. ASTER TIR bands were processed using radiometric calibration and thermal atmospheric correction.

The inclusion of both L8 and ASTER data was a deliberate decision to capitalize on the unique benefits of each sensor, resulting in a more robust and comprehensive set of evidence layers for the fuzzy logic model.

The L8 was primarily used for broad-scale lithological mapping. Its greater swath width (185 km) ensures excellent spatial coverage and uniformity, making it ideal for mapping vast geological units. Furthermore, its shorter wavelength visible and NIR bands (e.g.,

Coastal Aerosol, Blue, and Panchromatic) are especially useful for highlighting and mapping structural features such as faults and fractures because to their better spatial resolution (15-30 m) and sensitivity to topographic expression.

In contrast, ASTER was chosen because of its greater spectrum capabilities in the Short-Wave Infrared (SWIR) and Thermal Infrared (TIR) regions. The ASTER SWIR bands (Bands 4–9) have a high spectral resolution, which is necessary for distinguishing significant hydrothermal alteration minerals such as iron oxides (hematite), and clays (kaolinite), which are essential to the uranium mineralization scenario in Abu Harba. ASTER's TIR bands (Bands 10-14) may distinguish between silicate mineral groups (e.g., quartz vs. feldspars) and map larger lithological units depending on silica content.

As a result, the datasets are complementary: L8 gives improved wide lithological differentiation, whereas ASTER provides comprehensive mineralogical and alteration data. Their combined use overcomes the constraints of using either dataset alone, allowing for more confident identification of promising zones.

3.2 Image processing techniques

In the present investigation, numerous strategies employing distinct processes for increasing image quality are applied. These approaches incorporate optimum index factor (OIF), false color composites (FCC), band rationing (BR), independent component analysis (ICA), principal component analysis (PCA), minimum noise fraction transform (MNF), decorrelation stretch (DS) and image classification (IC).

3.2.1 OIF

The analysis using (OIF) assesses and ranks every conceivable Red-Green-Blue (RGB) color combination in multispectral remote sensing data, evaluating them according to their total variance and correlation coefficient (Chavez et al., 1984). OIF is calculated based on equation (1) (Chavez et al., 1984):

$$OIF = \frac{Std_i + Std_j + Std_k}{|Corr_{i,j}| + |Corr_{i,k}| + |Corr_{j,k}|} \quad (1)$$

Hereby Std_i is the standard deviation of a band i and $Corr_{i,j}$ is the absolute value of the correlation coefficient between two bands i and j . Selecting the three bands with the highest OIF ensures a combination that incorporates the most information, exhibiting minimal correlation. This choice is deemed to offer optimal information and is consequently employed for enhanced lithological distinction.

3.2.2 FCC

Enhancing the discrimination between the lithological and the hydrothermal alteration zones is achieved through techniques such as those suggested by Campbell et al. (2022). The use of false color composites (FCC) significantly aids in visualizing images, leading to improved interpretation. In this study, selection of RGB combinations is determined based on the exposed rock unit types, previous works,

outcomes of optimum index factor (OIF) analyses, and spectral characteristics of the datasets employed, ensuring the highest level of discrimination.

3.2.3 BR

The BR procedure entails dividing the digital number (DN) values of one band by the equivalent DN values of another band. The outcome is DN values are illustrated as a grayscale graphic, providing insights into the corresponding intensities of the bands. BR technique has proved advantageous for precise discrimination of lithological features and the qualitative identification of hydrothermal alteration (El-Raouf et al., 2023).

3.2.4 PCA

PCA is a well-known technique for reducing dimensionality, with the initial principal component capturing the highest achievable data variability. Consequently, the leading principal components exhibit the utmost variance and are predominantly employed to create resilient color composites, improving the visual depiction of surface components identification. In this study PCA is utilized for enhancing the lithological discrimination.

3.2.5 ICA

ICA exemplifies blind source separation, wherein it discerns source signals from mixed signals without requiring significant previous comprehension of the source signals or the mixing process. Hence, the goal of ICA is to recognize a set of uncorrelated elements that exhibit as much independence from each other as possible (Castella, 2024). As in PCA, ICA technique is implemented for better lithological discrimination.

3.2.6 MNF

MNF technique separates noise from spectral information in the data (Vermillion & Sader, 1999). L8 and ASTER bands in the original space are transformed into eigenspaces using MNF. The data space can be partitioned into two separate sections: one marked by significant eigenvalues and coherent eigenimages, whereas the other exhibits eigenvalues approaching unity and images predominantly influenced by noise. Enhancing spectral processing outcomes is possible by eliminating unwanted information and focusing only on coherent portions (Vermillion & Sader, 1999). The MNF bands were restored to their original data space, omitting the noise band(s), for bands with eigenvalues below 2, which were classified as noise.

3.2.7 IC

IC employs visual representations to generate thematic maps. The objective of classification is to discern distinctive attributes, patterns, or structures within an image and utilize them to allocate the image to a specific class. Choosing the right classifier is very important for making accurate lithological maps. Several algorithms were considered, including Random Forest (RF) and XGBoost, which are known for their high performance in classification tasks (Shebl et al., 2023). For this study, the Support Vector Machine (SVM) algorithm

was selected for several justified reasons. First, SVM works especially well when there isn't much training data because it tries to find the best separating hyperplane that maximizes the margin between classes. This makes it better at generalizing and reduces overfitting (Agrawal et al., 2024). This is a significant advantage because it is hard to get a lot of training pixels for each lithological unit in remote areas. Second, SVM works well in feature spaces with a lot of dimensions, like the multi-spectral input data used here (Mountrakis et al., 2010). Finally, recent comparative studies (e.g., Abdelkader et al., 2022) have shown once again that SVM is one of the most accurate classifiers for spectral lithological mapping using satellite imagery.

Thus, the present study aims to achieve precise and thorough lithological categorization by evaluating Landsat-8, ASTER, and Landsat-8+ASTER data, and identifying the most effective datasets for meticulous lithological mapping of the Abu Harba district.

Consequently, specific training datasets were identified for five different lithological classes and inputted into the SVM algorithm. The labeled dataset, comprising pixels extracted from known lithological units, was partitioned into a training set (70%) and an independent testing set (30%). This ratio is a conventional and effective standard in remote sensing applications, ensuring a substantial amount of data is available for the model to learn feature representations while retaining a statistically significant portion for unbiased evaluation (Abdelkader et al., 2022).

Definition of lithological classes was based on stringent criteria combining data from three sources, remote sensing results, field observations and existing high-resolution geological maps of the study area (Moussa et al. 2008). Representative and pure Regions of Interest (ROIs) were meticulously digitized for each defined class to form the labeled dataset.

Model validation was performed quantitatively using the held-out testing dataset (30%), which was not involved in the training or hyperparameter tuning process. The performance was evaluated using standard metrics derived from the confusion matrix, including Overall Accuracy (OA), and the Kappa coefficient.

3.3 Digital Elevation Model (DEM)

This study used a 12.5 m resolution DEM from the ALOS-PALSAR Terrain Corrected product, downloaded from the Alaska Satellite Facility (ASF) on 20 May 2023. Although part of the ALOS mission (JAXA, 2006–2011), the DEM is a modified SRTM dataset used for radiometric terrain correction rather than PALSAR-derived. The L-band SAR data from PALSAR enabled all-weather, day-night observations and repeat-pass interferometry. Such DEMs have proven effective for geological lineament extraction (Gaikwad et al., 2023).

3.3.1 Fill sink

Sink (and peak) is a term used to describe a common inaccuracy in (DEM) images. This error occurs due to resolution limitations or when elevation values are rounded to the nearest whole number. The fill sink approach was employed in the ArcGIS 10.9 environment to rectify sink issues in the ALOS-PALSAR (DEM) data of the research region.

3.3.2 Shaded relief

Shaded relief maps derived from DEM data visualize topography using grayscale gradients, where shadow boundaries may indicate lineaments (El-Raouf et al., 2023). A thematic shaded relief map was generated in ArcMap using a sun azimuth of 315° (NW) and 45° elevation angle, optimized to enhance contrast between illuminated and shadowed terrain features.

3.3.3 Lineament extraction

The PCI Geomatica 2014 software was utilized to autonomously obtain lineaments from the shaded relief imagery derived from the DEM. The two fundamental processing processes employed to perform automated lineament extraction are outlined below. The initial phase involves identifying edges that signify areas of abrupt variations in the values of adjacent pixels, followed by the subsequent step of detecting the presence of lines (Adiri et al., 2017). These processes mostly employ the PCI Geomatica software's LINE module, a popular package for automatically extracting lineaments.

3.4 AGRS data

The study area was covered by an AGRS and magnetic survey conducted by (Aero -Service, 1984) to assess mineral, oil, and groundwater potential in northern Egypt. The survey comprised NE-SW flight lines (45°/225° azimuth) spaced 1.5 km apart, with NW-SE tie lines (135°/315°) at 10 km intervals. Data were acquired at 120 m mean terrain clearance and 220–315 km/h speed using a high-sensitivity 256-channel gamma-ray spectrometer (Hisens AGRS 3000F), measuring U, Th, and K decay. Processed gamma-ray data were presented as 1:50,000 scale contour maps based on topographic and photomosaic basemaps.

3.4.1 Georeferencing and map projections

The gamma-ray spectrometric data, originally in Egypt Red Belt Transverse Mercator (Helmert 1906), were reprojected to UTM WGS-84 using ArcGIS 10.9 to align with remote sensing datasets (IAEA, 2003).

3.4.2 Gridding

The gamma-ray spectrometric data were gridded at 30 m resolution using a bi-directional spline interpolation algorithm in Surfer® (Golden Software, LLC) to match the multispectral data spatial resolution. This method efficiently accounts for correlations between adjacent flight lines during interpolation (Billings & FitzGerald, 1998).

3.4.3 Image presentation

The grid values were scaled to the dynamic range (usually 256 greyscale levels between 0 and 255) in order to render the gridded AGRS data (Total Count (TC), K, U, and Th). The grid values control the brightness of the individual components of the display device, known as pixels, resulting in a grayscale image (IAEA, 2003). The conversion of the gridded data to grayscale images was conducted using the ENVI software version 5.3 by L3Harris Geospatial USA (Broomfield, CO, USA).

3.4.4 Ternary radioelement maps

A ternary radioelement map represents K (red), Th (green), and U (blue) concentrations through RGB composite imaging (IAEA, 2003). Due to U channel noise and reduced human sensitivity to blue intensity variations (IAEA, 1997), sum-normalization was applied to calculate relative K, Th, and U concentrations before visualization.

$$K_n = \frac{K}{K+Th+U}$$

$$Th_n = \frac{Th}{K+Th+U}$$

$$U_n = \frac{U}{K+Th+U}$$

This process transforms the concentrations of radioelements into their respective relative abundances (Kovarch et al., 1994).

3.5 Fuzzy logic modeling (FLM)

GIS based FLM is an overlay analysis technique for continuous spatial evidence layers (raster). It makes the assumption that the geometry and characteristics of spatial data are flawed, particularly that class borders are inaccurate. FLM deals with situations when class boundaries are ambiguous, focusing on possibilities rather than probabilities (Shawky et al., 2019). Each continuous evidence layer (e.g., lineament density, alteration) was transformed into a fuzzy membership surface through a process called fuzzification. This process converts the original input values into a normalized Fuzzy Membership Value (μ), which ranges from 0 to 1.

$\mu \approx 1$ indicates that the conditions at a given pixel are highly favorable for the target mineralization.

$\mu \approx 0$ indicates that the conditions are highly unfavorable.

Values between 0 and 1 represent intermediate or gradational favorability.

This μ value represents the degree to which a pixel belongs to the fuzzy set of 'prospective areas' based on that specific evidence layer. The choice of the fuzzification function (e.g., linear, sigmoidal, J-shaped) for each layer was based on the known spatial relationship between the measured parameter and uranium mineralization, as derived from the conceptual model and analysis at known deposit sites.

Fuzzy membership functions, which indicate the extent to which a location belongs to a favorable set, provide the foundation for converting continuous spatial data into normalized, commensurate layers of prospectivity in a Geographic Information System (GIS). These functions, encompassing categories such as Large, Small, Linear, and MS Small, mathematically delineate the correlation between an input raster's original values and a resultant fuzzy membership score (μ) that spans from 0 (entirely unfavorable) to 1 (entirely favorable).

Large function allocates elevated μ values to greater input values, which is optimal for criteria such as the geochemical concentration where higher values are preferable. In contrast, a Small function allocates elevated μ values to lesser input numbers, ideally applicable to factors like distance to structures, where closeness is beneficial. The MS Large and MS Small functions are specialized membership types

belonging to a category known as Monotonic or Sigmoidal functions. Unlike simpler linear functions, they are designed to model a more gradual, non-linear, and often more realistic transition between non-membership ($\mu=0$) and full membership ($\mu=1$). Both functions are defined by two threshold parameters: a midpoint (which defines the value at which the membership score μ is exactly 0.5) and a spread (which controls the steepness of the transition around the midpoint). Their sigmoidal form facilitates nuanced, non-linear modeling of geological relationships, thereby reflecting expert knowledge more accurately than binary or linear approaches (De Souza Gaia and De Souza Filho, 2023).

The selection of MS Large and MS Small fuzzy membership functions in this prospectivity model was explicitly guided by the conceptual genetic model for fracture-fill uranium mineralization. The (MS Large) function was applied to evidence layers where increasing values correlate directly with higher favorability. This included the (host rock or metal source) criterion, specifically the SVM-derived lithological probability of alkali feldspar granite, as well as airborne uranium and total count gamma-ray measurements, where higher values indicate greater geochemical fertility and radiogenic character. It was also applied to the (pathway) criterion (lineament density), where a higher density of fractures enhances fluid flow potential, and the (trap) criterion (U/Th ratio and alteration anomaly intensity), where elevated values are key indicators of geochemical redistribution and hydrothermal alteration. Conversely, the (MS Small) function was deliberately chosen for topographic layers (elevation and slope) based on the empirical observation that in the arid, erosional environment of the Abu Harba district, known fracture-controlled uranium occurrences are preferentially exposed and preserved in (low-lying, gentle terrain). This inverse relationship, where smaller topographic values correspond to higher prospectivity, is precisely and effectively modeled by the MS Small function. This rigorous, criteria-specific application of fuzzy functions ensures the model accurately translates the underlying geological principles into a quantitative spatial prediction.

Following the fuzzification of individual evidence layers, the fuzzy membership values (μ) for each pixel across all rasters were integrated using a set of fuzzy operators to produce a final prospectivity map. The selection of an appropriate operator is critical, as each implements a distinct mathematical rule to combine memberships, thereby reflecting a specific logical relationship between the geological criteria.

Fuzzy operators provide the logical framework for integrating fuzzified evidence layers, with the choice of operator reflecting the specific geological relationship between criteria. The Fuzzy And operator, defined as $\mu_{\text{combination}} = \min(\mu_1, \mu_2, \dots, \mu_n)$, is applied when the simultaneous presence of all factors is essential, as it returns the minimum value and thus requires all inputs to be high to produce a high output. Conversely, the Fuzzy or operator, expressed as $\mu_{\text{combination}} = \max(\mu_1, \mu_2, \dots, \mu_n)$, is employed where the presence of any single favorable factor is deemed sufficient, as it returns the maximum value from the input rasters. For more nuanced integration, compensatory operators are utilized. The Fuzzy Algebraic Sum ($\mu_{\text{combination}} = 1 - [(1 - \mu_1) * (1 - \mu_2) * \dots * (1 - \mu_n)]$) combines evidence where the presence of any factor is highly favorable and the combined evidence increases the overall membership value. In contrast, the Fuzzy Algebraic Product ($\mu_{\text{combination}} = (\mu_1 * \mu_2 * \dots * \mu_n)$) is used where the simultaneous presence of factors is crucial, as the absence of any one factor significantly decreases the output. A parameterized compromise between these effects is achieved with the Fuzzy Gamma operator, defined as $\mu_{\text{combination}} = (\text{Fuzzy Algebraic Sum})^{\gamma} * (\text{Fuzzy Algebraic Product})^{(1-\gamma)}$. A gamma (γ) value of 0.75 was selected for

the final integration of major factor groups in this study, striking a balance between the increasing tendencies of the Fuzzy Sum and the decreasing effects of the Fuzzy Product. This reflects the geological premise that while the presence of individual factors is important, their synergistic coexistence is the most compelling indicator of prospectivity. Consequently, the selection of each operator was deliberately based on the logical relationship between layers, thereby mirroring the geological processes governing uranium mineralization.

Conceptual summaries and organization of all the previously employed approaches are presented in Fig. 2.

4 Results

4.1 Image processing results

4.1.1 OIF and FCC

The FCC approach optimally combines three bands (Red, Green, Blue) to minimize correlation and maximize variance. For L8 (bands 7,6,1) and ASTER (bands 1,8,9), selected based on highest OIF values (Table 1), effectively discriminated AFG units (Fig. 3a, b).

4.1.2 BR

Band ratios (BRs) were selected based on material spectral properties and absorption-to-reflectance ratios (Sabins, 1999). For L8 data, RGB composites of 4/2 (iron oxide, red), 6/7 (clay/hydroxyl, green), and 6/5 (ferrous minerals, blue) effectively mapped lithological and alteration zones (Ali and Pour 2014; Fig. 4a). An alternative L8 composite (6/7, 6/5, 5) distinguished AFG (green) and SYG (violet) granitoids (Fig. 4b). ASTER ratios (4/7, 3/4, 2/1;) and (4/7, 4/1, 2/3*4/3) highlighted AFG (blue) and SYG

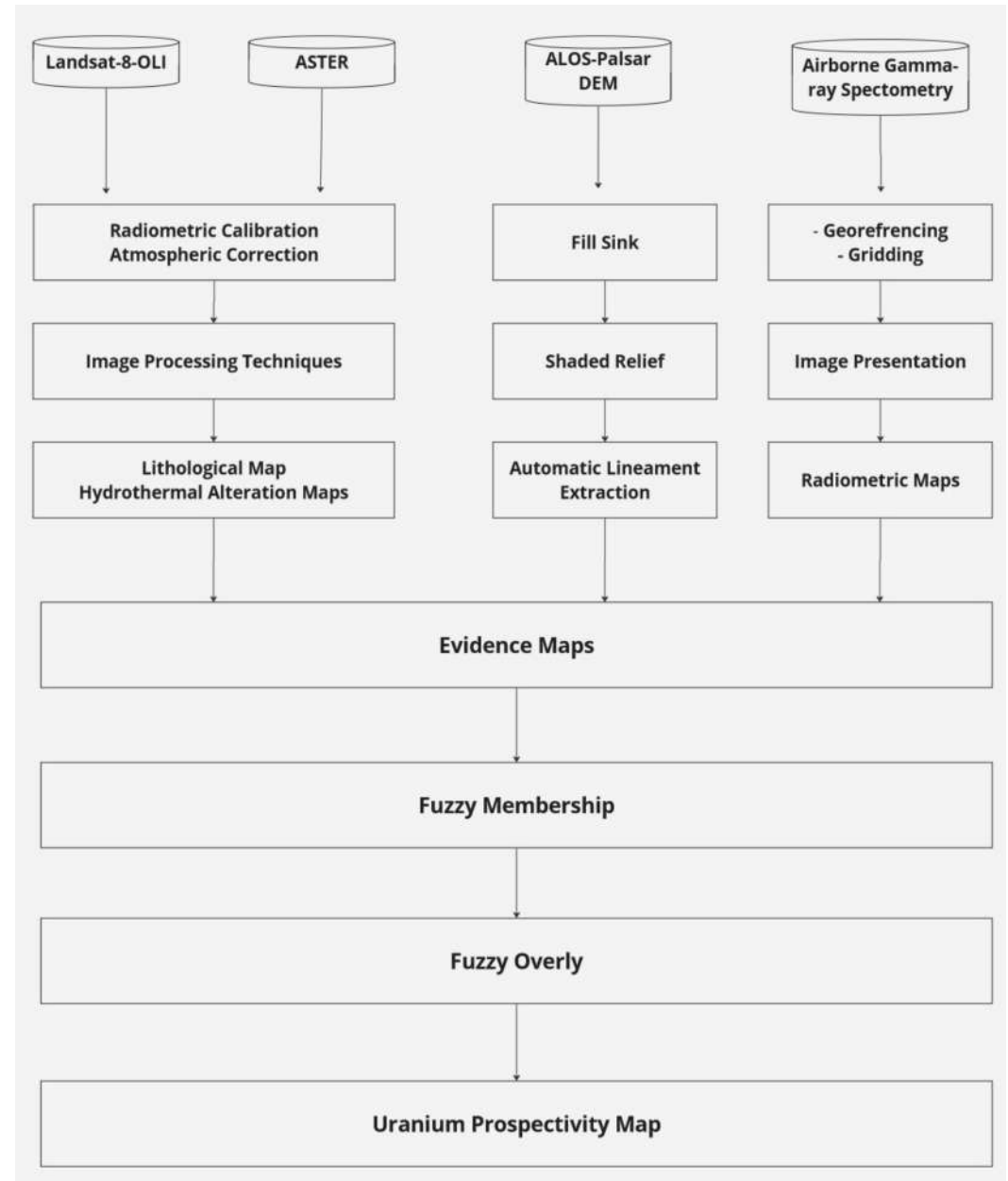


Fig.2. Flowchart showing the steps of the proposed processes.

(violet) (Fig. 4c,d). Ferrugination and kaolinite were identified using ASTER b4/b3 (Fig. 5a) and 7/5 (Fig. 5b), respectively, with density slicing revealing their predominance in AFG (Fig. 5c,d).

Table. 1: Highest values of OIF and ranks of combinations of Landsat-8 and ASTER bands

Landsat-8					ASTER				
Combination of Bands			Rank	OIF	Combination of Bands			Rank	OIF
b1	b6	b7	1	(74.02)	b1	b8	b9	1	(77.25)
b1	b5	b7	2	(73.79)	b1	b7	b9	2	(77.03)
b1	b5	b6	3	(72.48)	b1	b5	b9	3	(76.80)
b1	b4	b7	4	(72.28)	b1	b6	b9	4	(76.79)
b1	b4	b6	5	(72.17)	b1	b7	b8	5	(76.34)
b1	b2	b7	6	(72.09)	b1	b5	b8	6	(76.10)

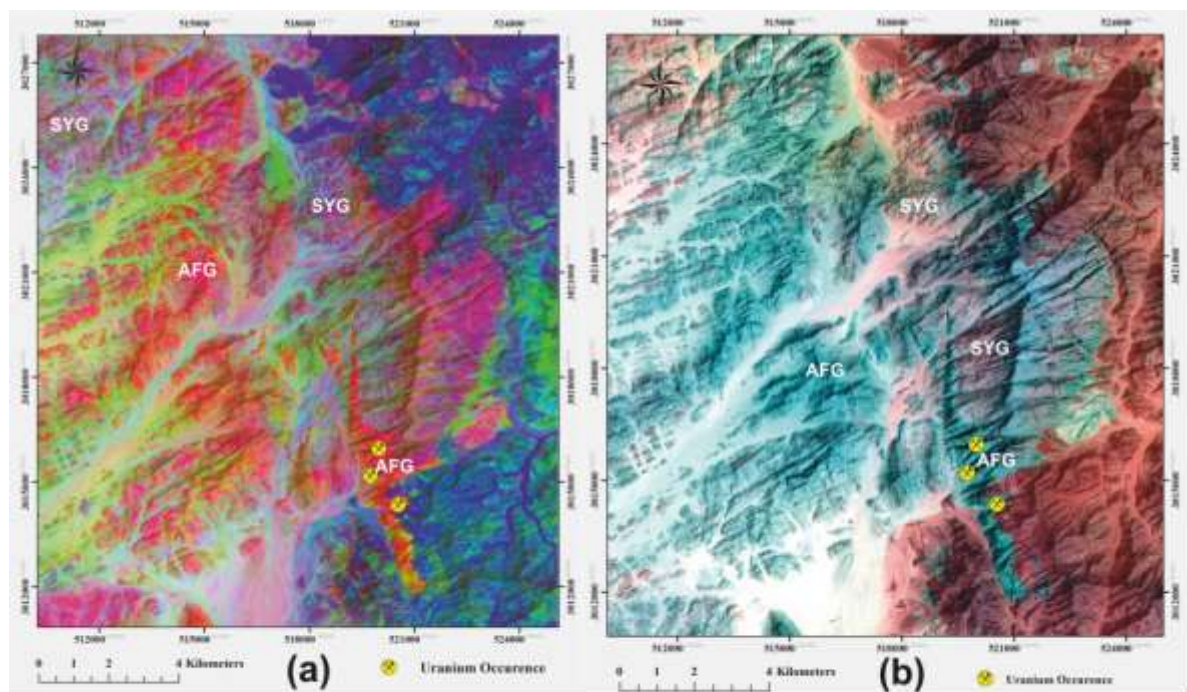


Fig.3: (a) False color composite image (FCC) of landsat-8 OLI (L8) bands 7,6,1 in RGB. (AFG= Alkali feldspar granite), (SYG= Syenogranite), (DV= Dokhan volcanics), (MV= Metavolcanics), (WD= Wadi deposits). (b) FCC image of ASTER bands 1,8,9 in RGB.

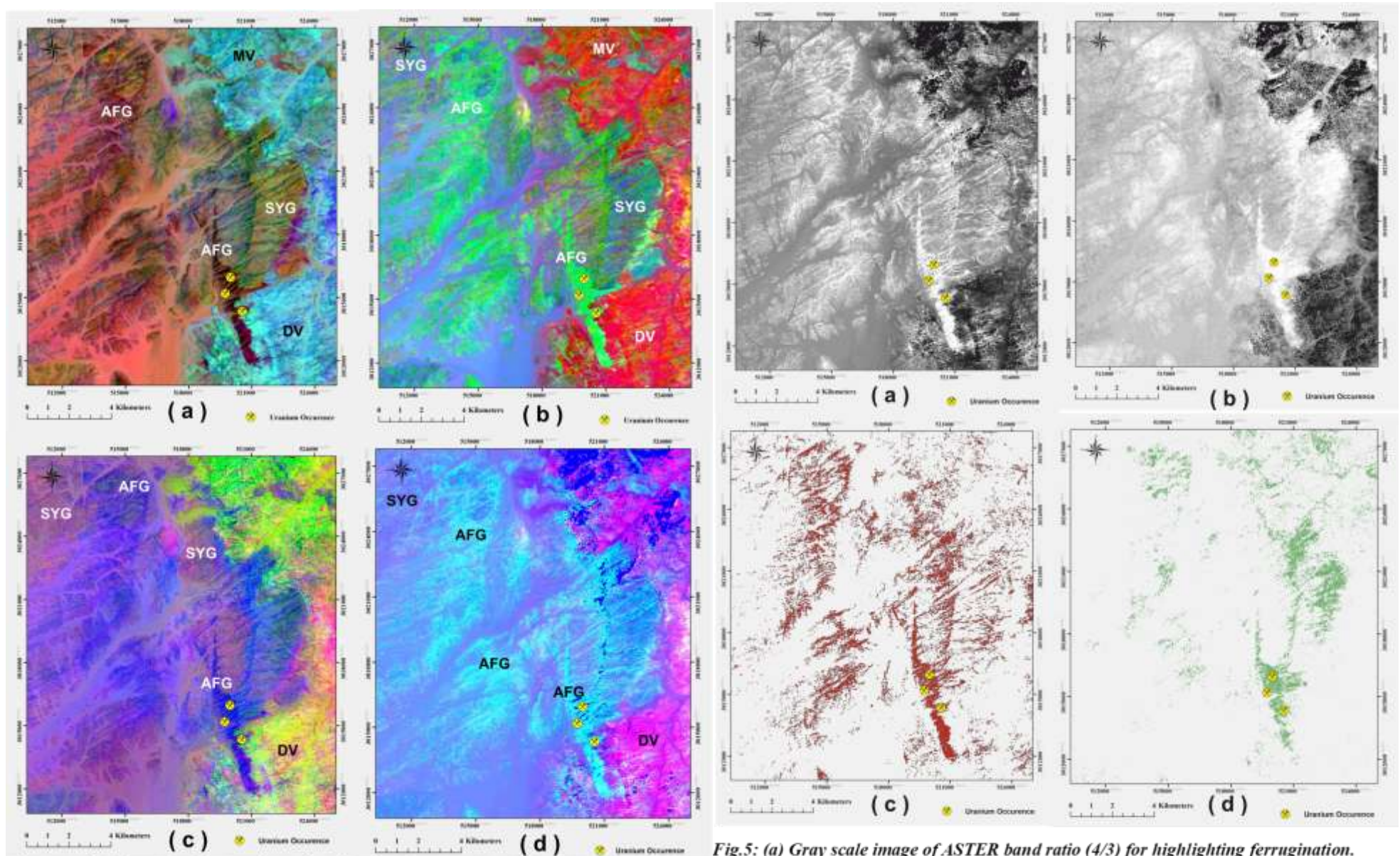


Fig.4: (a) Sabins ratios for Landsat-8 OLI band ratios (4/2, 6/7, 6/5) in RGB.
 (b) FCC image of L8 band ratios 6/7, 6/5, and 5 in RGB.
 (c) FCC image of ASTER band ratio (4/7, 3/4, 2/1) in RGB as proposed by (Abdeen, M.M., Allison, T.K., Abdelsalam, M.G., Stern, R.J. 2001).
 (d) FCC image of ASTER band ratios (4/7, 4/1, 2/3 * 4/3).

Fig.5: (a) Gray scale image of ASTER band ratio (4/3) for highlighting ferrugination.
 (b) Gray scale image of ASTER band ratio (7/5) for highlighting kaolinite.
 (c) Image map showing ferrugination alteration in red color extracted from ASTER band ratio (4/3) by density slicing technique.
 (d) Image map showing kaolinite alteration in green color extracted from ASTER band ratio (7/5) by density slicing technique.

4.1.3 PCA-ICA

PCA and ICA transformations enhance spectral discrimination of rock units through dimensionality reduction (Abdelkader et al., 2022). For L8, the PC1-PC2-IC1 RGB composite distinguished AFG (red) and SYG (green) (Fig. 6a), while ASTER's PC1-PC2-IC9 combination highlighted AFG in deep red (Fig. 6b). The integrated PCA-ICA approach demonstrates superior noise reduction compared to individual applications.

4.1.4 MNF

The MNF transformation of L8 and ASTER data effectively enhanced lithological discrimination, with MNF1-MNF2-MNF3 bands demonstrating optimal separation. The L8 composite (MNF1-2-3 in RGB) distinctly identified AFG (red) and SYG (violet) (Fig. 7a), while ASTER's equivalent combination highlighted AFG in forest green (Fig. 7b).

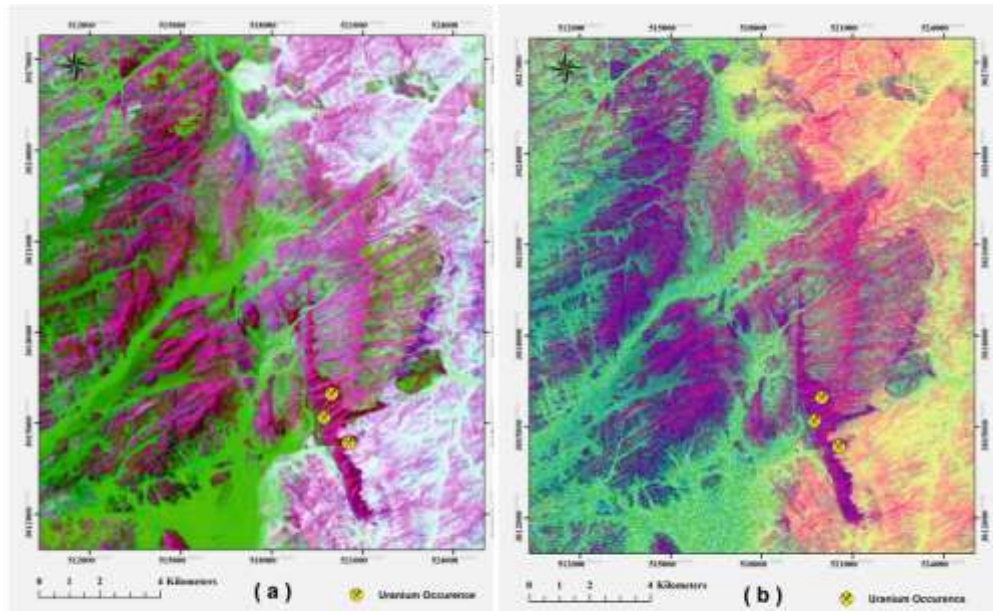


Fig. 6: (a) FCC image of L8 (PC1-PC2-IC1) in RGB. (b) FCC image of ASTER (PC1-PC2-IC9) in RGB.

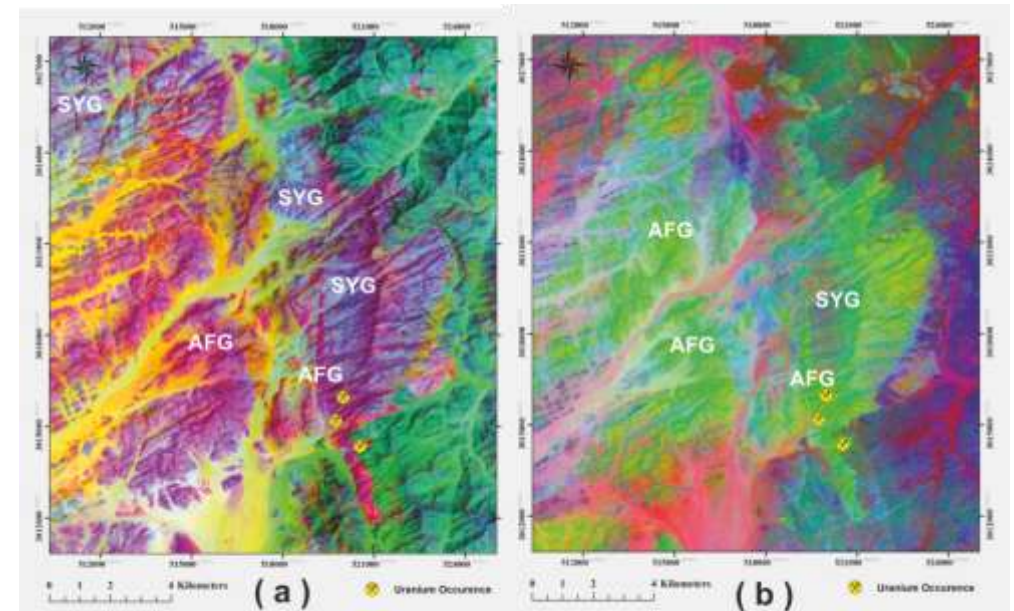


Fig. 7: (a) FCC image of L8 (MNF1-MNF2-MNF3) in RGB. (b) FCC image of ASTER (MNF1-MNF2-MNF3) in RGB.

4.1.5 SVM

SVM-based lithological classification of L8, ASTER, and combined datasets successfully identified five units (MV, DV, SYG, AFG, WD), though with notable discrepancies. The combined L8+ASTER dataset achieved superior accuracy (OA=86.21%, K=0.81) compared to individual datasets (Table 2). Optimal results were obtained using SVM on PCA-transformed L8+ASTER data (OA=98.07%, K=0.97), with exceptional class-specific accuracy (e.g., UA=99.56% for AFG, 99.68% for SYG), validated against field observations and existing geological maps (Fig. 8).

Table 2: Kappa coefficient, producer, user, and overall accuracies of SVM tested datasets

Classes	L8- bands		ASTER- bands		L8+ASTER		L8-PCA		ASTER-PCA		L8+ASTER- PCA	
	PA	UA	PA	UA	PA	UA	PA	UA	PA	UA	PA	UA
WD	100.00	83.73	100.00	80.72	99.34	98.83	100.00	98.74	100.00	95.15	100.00	100
AFG	99.42	68.95	98.84	64.39	67.36	72.10	98.26	60.57	99.42	73.08	99.56	99.56
SYG	40.43	76.23	26.52	96.83	90.58	87.86	50.43	85.93	65.65	99.34	99.68	99.68
DV	80.16	92.52	90.69	88.54	65.46	90.20	78.14	93.24	93.52	90.23	96.27	96.03
MV	87.35	85.29	82.53	85.63	91.61	70.16	89.76	78.42	84.94	89.81	96.98	97.17
Tot	OA= 81.57	K= 0.76	OA= 80.24	K= 0.74	OA= 86.21	K= 0.81	OA= 83.34	K= 0.79	OA= 89.28	K= 0.86	OA= 98.07	K= 0.97
Support Vector Machine (SVM), Overall Accuracy (OA), kappa coefficient (K), Producer Accuracy (PA), User Accuracy (UA), Total number (Tot)												

4.2 DEM

The lineament map revealed predominant NE-SW and E-W structural trends (Fig. 9a), consistent with regional patterns (Hamimi et al., 2023). Density and intersection analyses identified zones of concentrated lineaments (Fig. 9b,c), with uranium occurrence correlating to high-density intersections. A slope map (degrees) was generated to analyze topographic gradients (Fig. 9d).

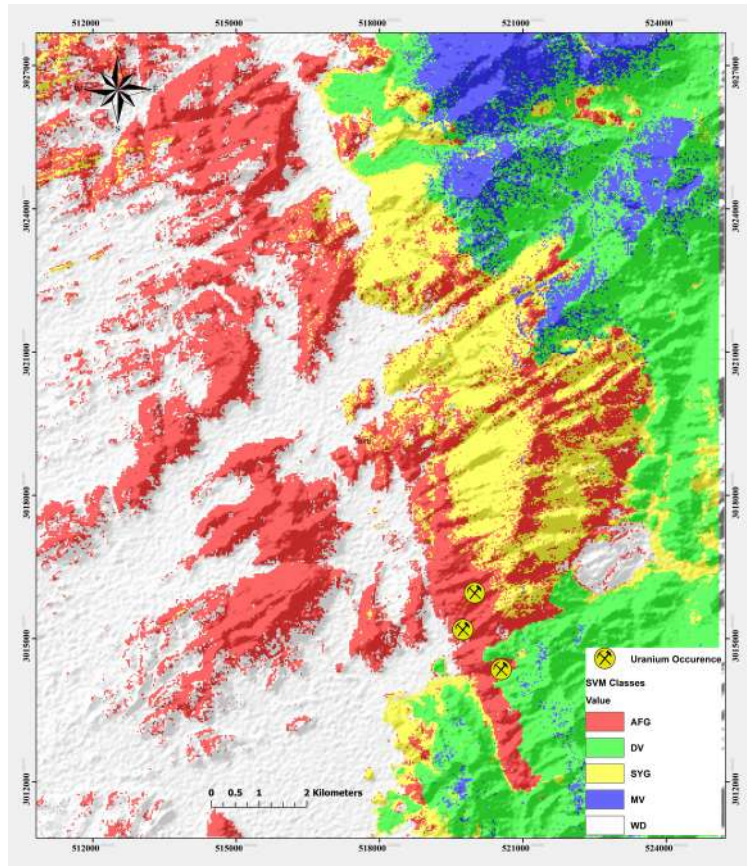


Fig.8. Thematic map based on SVM of PCA (L8+ASTER) bands

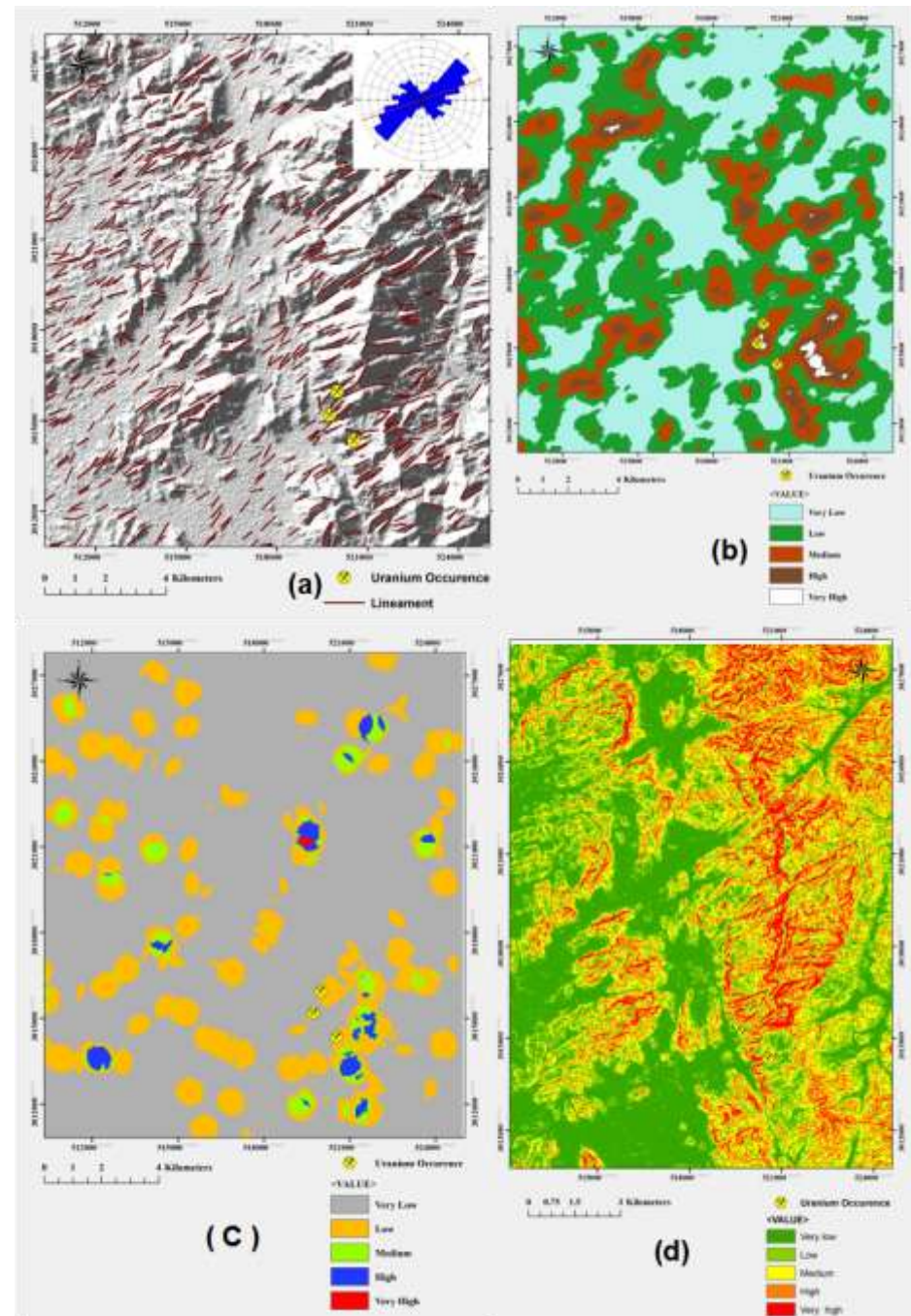


Fig.9: (a) Shaded relief topography map of Abu Harba district showing lineament and their trends. (b) Lineament density map of Abu Harba district. (c) Lineament intersection density

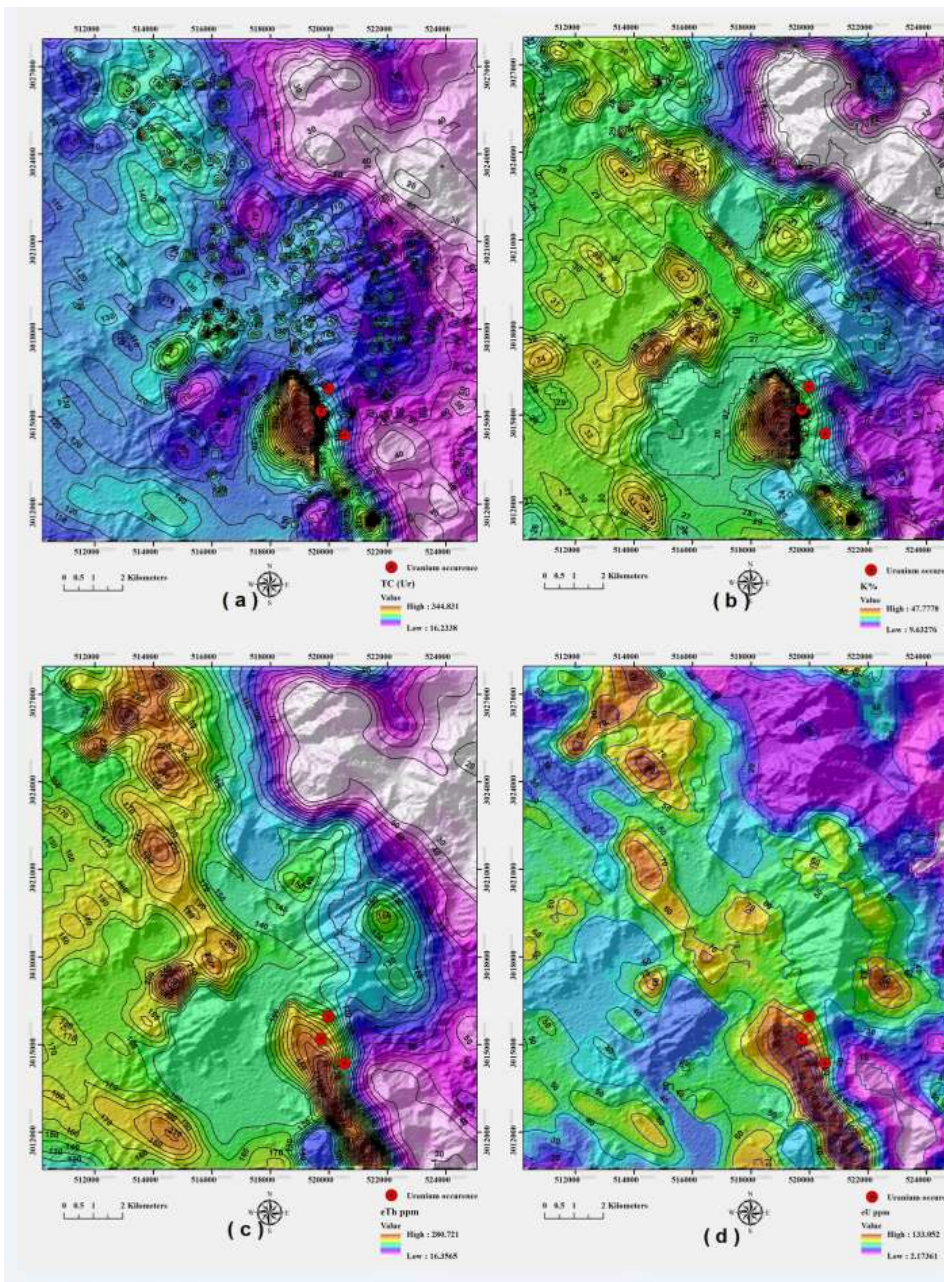


Fig.10: (a) Total-count contour map in Ur, Abu Harba district. (b) Potassium contour map in %, Abu Harba district. (c) Equivalent uranium contour map in ppm, Abu Harba district.

4.3 AGRS

4.3.1 Total-count and radio-elements maps

The radiometric contour maps (TC, K%, eU, eTh) show elevated levels in granitic terrains (Fig. 10), with AFG exhibiting the highest concentrations, reflecting its differentiated nature (Bea, 1999). While radioactivity varies significantly between rock types and locally within units, lithological boundaries remain discernible despite occasional gradational contacts.

4.3.2 Ternary or (composite) image maps

This study analyzes two ternary composites: (1) a radioelement map (K-eU-eTh) showing granitic rock correlations, with AFG displaying elevated values (bright colors) linked to uranium mineralization (Fig. 11a); and (2) a uranium enrichment map (eU-eU/eTh-eU/K) highlighting anomalous zones through high ratio values (bright areas) within AFG (Fig. 11b). The latter effectively identifies uranium migration patterns.

4.4 FLM

The final uranium prospectivity map for the Abu Harba district (Fig. 12) was generated through the integration of fuzzified evidence layers, each representing a critical component of the established genetic model, using a sequence of specifically chosen fuzzy operators (De Souza Gaia & De Souza Filho, 2023). The host rock component was synthesized by combining the SVM-derived alkali feldspar granite (AFG) probability layer with fuzzified airborne total count (TC) and equivalent uranium (eU) measurements all transformed using the MS Large function to reflect increasing favorability via a Fuzzy Algebraic Sum operator to identify areas exhibiting a synergistic combination of source rocks and geochemical fertility. The pathway component was represented by a lineament density layer, also fuzzified with an MS Large function to emphasize zones of highest fracture density. For the trap component, key indicators including the eU/eTh ratio (MS Large), alteration anomalies (MS Large), and topo-

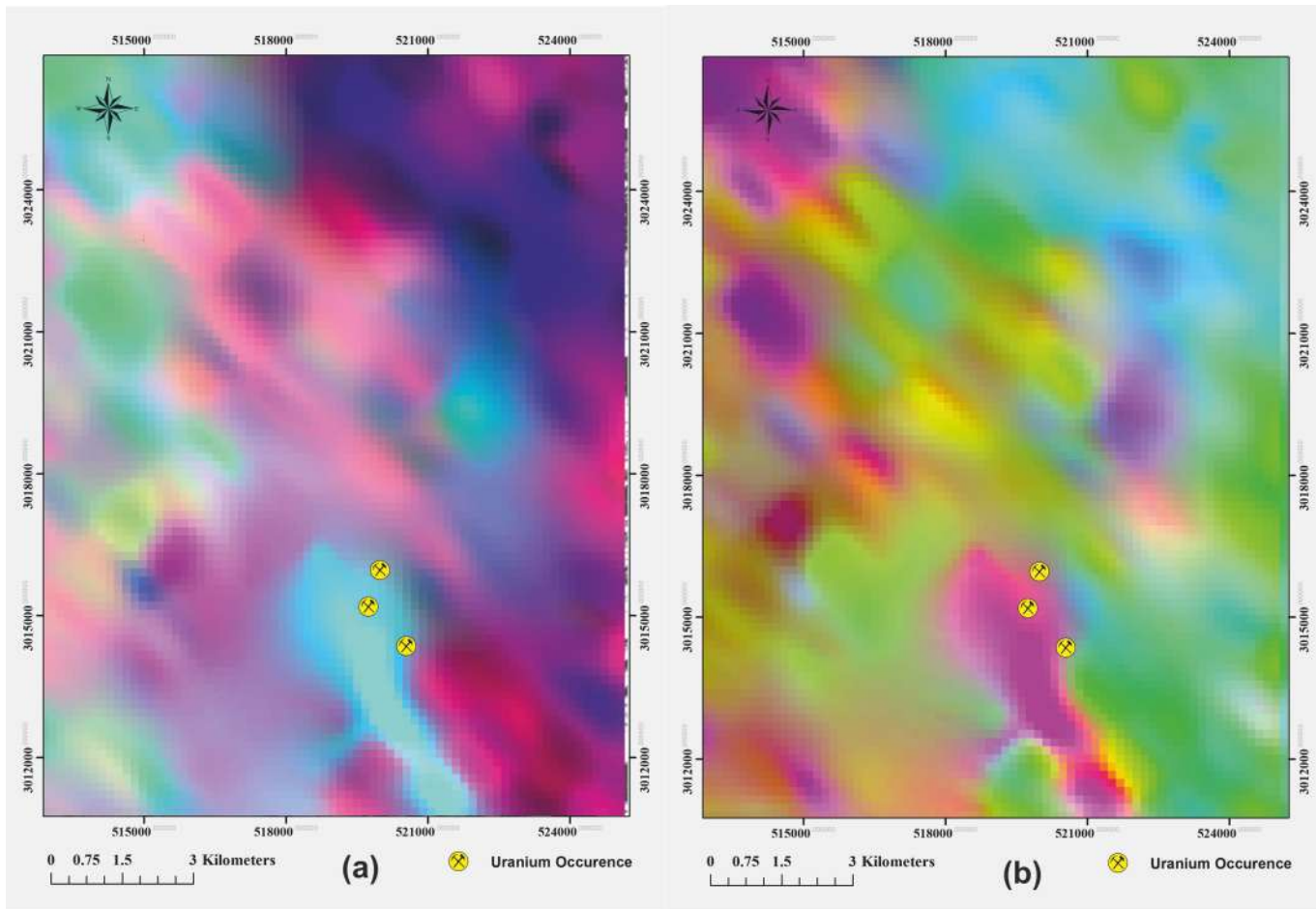


Fig.11: (a) *K-eTh-eU image map in RGB, Abu Harba district.*
 (b) *eU- eU/eTh- eU/K image map in RGB, Abu Harba district.*

graphic features, elevation and slope (both MS Small, where lower values are more favorable) were amalgamated using a Fuzzy Algebraic Sum to highlight areas where geochemical trapping and favorable preservation conditions coincide. The integration of these three major components was performed using a Fuzzy Gamma overlay ($\gamma = 0.75$), achieving an optimal balance between the increasing effect of the Fuzzy Sum and the restrictive effect of the Fuzzy Product, thereby modeling the essential geological premise that while individual factors are important, their spatial coexistence is paramount (Table.3). The resulting prospectivity map was classified into five distinct priority levels. The model validation is strongly demonstrated by the precise spatial correlation of all known uranium occurrences (U.1, U.2, U.3) within the delineated high to very high potential zones.

Table.3: Summary of parameters used in the fuzzy logic modeling process.				
Mineral System Parameters	Evidence Map	Fuzzy Membership	Fuzzy Operators	Integrative Fuzzy Overlay Operative
Host Rock (Metal Source)	SVM classification of multispectral data and airborne gamma ray spectrometry (TC & eU)	MS Large (TC & eU)	SUM	GAMMA, Index 0.75
Pathways	Density of lineaments extracted from DEM.	MS Large	-	
Trap	eU/eTh	MS Large	SUM	
	Elevation	MS Small		
	Slope	MS Small		
	Alteration (ferrugination & kaolinization)	MS Large		

5 Discussion

The Abu Harba uranium deposits demonstrate fracture-hosted mineralization in post-collisional A-type granites (595–605 Ma) of the ANS. Uranium frequently occurs in refractory minerals (zircon, allanite) in the alkali feldspar granite (AFG) phase and takes approximately 200 Myr of metamictization to be mobilized (Cuney, 2014). This delay explains the substantial link between NE-SW fracture networks and uranium distribution, as fractures served as conduits for supergene fluids during Quaternary reactivation (Osmond et al., 1999).

The uranium mineralization system comprises of three key components: metamictized U-bearing silicates in AFG (source; (Cuney, 2014)), NE-SW fractures (pathways; Hamimi et al., 2023), and hematite-kaolinite alteration zones with low topography and gentle slopes (traps). The interplay of these components defines a coherent genetic model that accounts for the mobilization, transport, and subsequent deposition of uranium.

The Schlagintweit uranium deposit in Argentina's Sierra Los Gigantes is a typical fracture-fill uranium system, with hexavalent uranium minerals leached from the Achala batholith granite (329 Ma) and deposited along fractures during Quaternary supergene episodes (Dahlkamp, 2010). This system, similar to Abu Harba's mineralization (595-605 Ma granite source), demonstrates: (1) metamictization of U-bearing minerals during the prolonged pre-mineralization period, (2) fracture networks as fluid pathways and physical traps, and (3) hematite-kaolinite alteration serving as chemical traps via uranium adsorption (Shuibo et al., 2009; Issa et al., 2023). The similarity sup-

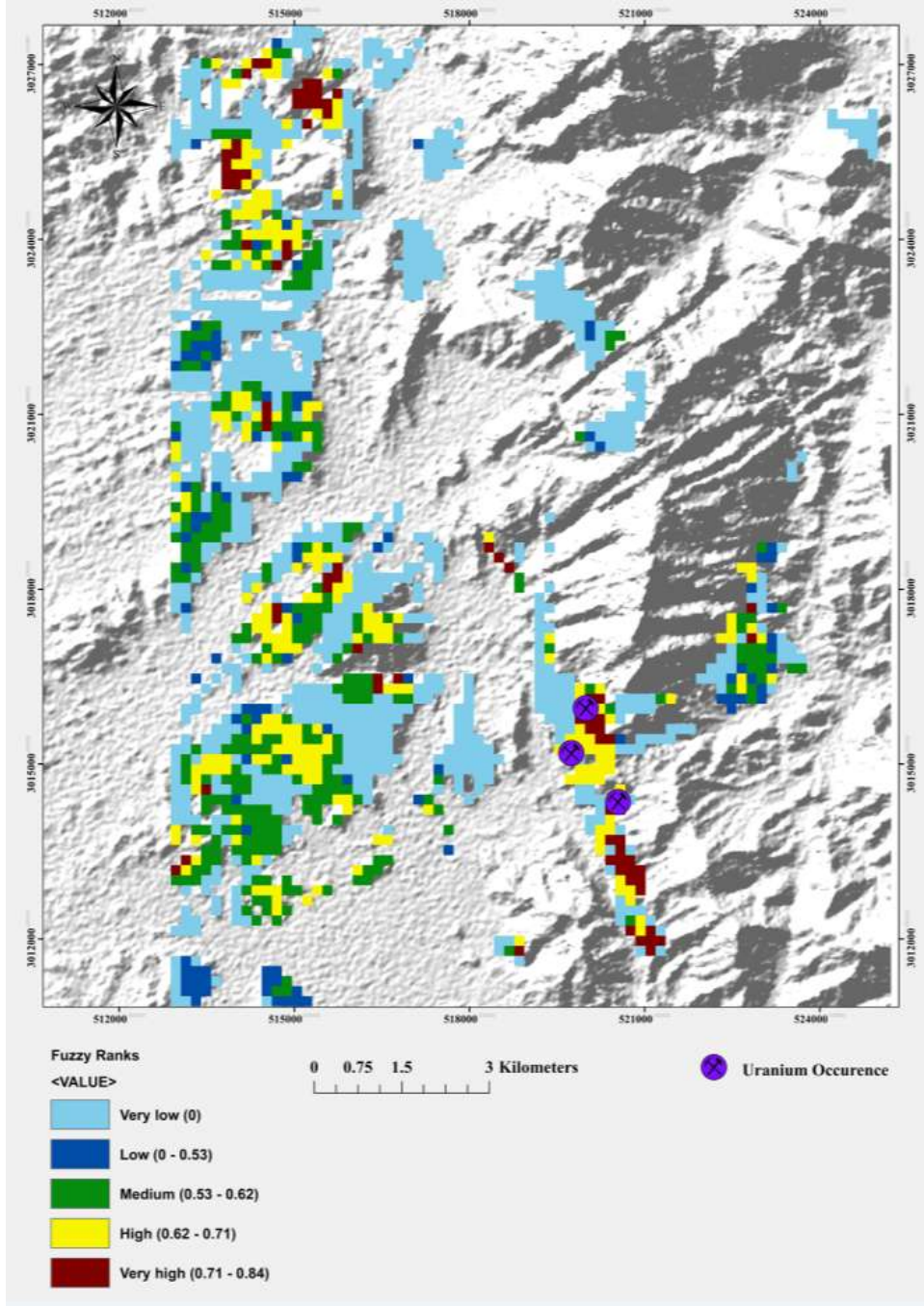


Fig. 12 Uranium prospectivity map of Abu Harba district

ports Abu Harba's categorization as a fracture-fill system (IAEA, 2020), in which topographic depressions and Fe-oxide coatings encourage uranium accumulation via uranyl phase precipitation.

FLM effectively managed Abu Harba's exploration challenges, attaining high accuracy in forecasting uranium occurrences while minimizing survey costs by removing 82% of non-prospective areas. Economically, the method permits sustainable exploitation of small deposits (~2,000 t U₃O₈; Cuney & Kyser, 2016) by targeting high-probability zones (U.1-U.3) and cutting discovery costs below \$0.50/lb U₃O₈. This generates a transportable template for similar terrains throughout the ANS.

The predictive accuracy of the final prospectivity model was primarily validated by its successful delineation of all known uranium occurrences (U.1, U.2, U.3) within the high and very high potential zones (Figure 12). This strong spatial correlation provides a high degree of confidence in the model's effectiveness and confirms that the integrated criteria accurately reflect the geological controls on mineralization in the Abu Harba district. However, field validation of the newly identified high-potential targets presents significant logistical challenges. The remote location and extremely rugged topography of the study area hinder site access and comprehensive ground-truthing efforts. These constraints represent a primary limitation of this study.

Consequently, the high and very high potential zones identified here should be considered high-priority targets for future, focused ground-based exploration campaigns. This model serves to significantly de-risk future exploration by providing a data-driven framework for prioritizing specific areas within this vast and remote district.

6 Conclusion

The present study successfully developed an effective FLM for uranium exploration in the Abu Habra district by integrating multi-sensor remote sensing and airborne gamma-ray data. This study directly addresses a significant research deficiency by providing a tailored, cost-effective framework for the examination of fracture-filled uranium deposits in the challenging and arid terrains of the ANS.

The primary geological factors that bolster this methodology are (1) uranium enrichment is structurally controlled in hematite-kaolinite altered zones of low-topography alkali feldspar granites, (2) NE-SW fault systems served as the principal conduits for fluids, and (3) the alkali feldspar granites constituted the principal source of uranium.

The developed (FLM) demonstrated high predictive efficiency, successfully eliminating 82% of the study area as non-prospective while accurately delineating all known mineralized occurrences (U.1–U.3). The model's validity was further substantiated by its strong alignment with the established geological characteristics of the Schlagintweit deposit in Argentina, a key analogue for this deposit type. The principal novelty of this research lies in its development of a robust, repeatable prospectivity methodology that utilizes widely accessible satellite and geophysical data. This approach significantly reduces exploration risk in remote regions by transitioning from a qualitative assessment to a quantitative, data-driven integration, thereby providing a scalable foundation for future uranium exploration across the (ANS). Although the target deposits are relatively small (~2,000 t U₃O₈), the methodology proves highly effective in prioritizing zones with the highest potential, offering a cost-effective strategy for exploring this challenging deposit style.

Future work should integrate high-resolution surveys to further enhance predictive accuracy. Specifically, uncrewed aerial vehicle (UAV)-borne gamma-ray spectrometry flown at low altitudes could dramatically improve the resolution of radiometric measurements, targeting subtle anomalies associated with mineralization. Furthermore, LiDAR surveys are recommended to generate high-resolution digital elevation models capable of mapping subtle geological structures and fracture networks obscured by surface debris. The subsequent integration of these high-fidelity datasets with hyperspectral data and machine learning algorithms will be critical for augmenting the model's resolution and predictive precision.

Acknowledgments

The author expresses gratitude for the logistical help offered by the Nuclear Materials Authority of Egypt (NMA). The Exploration Division of NMA deserves special thanks for supplying the airborne gamma ray spectrometry data. The author expresses gratitude to U.S. NASA and Alaska Satellite Facility for supplying the remote sensing data. The author also much appreciates editors' and reviewers' valuable and deep comments.

References:

- ABDELKADER, M.A., WATANABE, Y., SHEBL, A., EL-DOKOUNY, H.A., DAWOUD, M., CSÁMER, Á. “Effective delineation of rare metal-bearing granites from remote sensing data using machine learning methods: A case study from the Umm Naggat Area, Central Eastern Desert, Egypt.” *Ore Geology Reviews* 150 (November 1, 2022): 105184. <https://doi.org/10.1016/j.oregeorev.2022.105184>.
- ADIRI, Z., HARTI, A.E., JELLOULI, A., LHISSOU, R., MAACHA, L., AZMI, M., ZOUHAIR, M., BACHAAOUI, E.M. “Comparison of Landsat-8, ASTER and Sentinel 1 satellite remote sensing data in automatic lineaments extraction: A case study of Sidi Flah-Bouskour inlier, Moroccan Anti Atlas.” *Advances in Space Research* 60, no. 11 (December 1, 2017): 2355–67. <https://doi.org/10.1016/j.asr.2017.09.006>.
- AERO -SERVICE. “Final report on Airborne Magnetic and Radiation survey in Eastern Desert, Egypt. Work completed for the Egyptian General Petroleum Corporation (EGPC).” Huston, Texas, United States of America: Western Geophysical Co., 1984.
- AGRAWAL, N., GOVIL, H., CHATTERJEE, S., MISHRA, G., MUKHERJEE, S. “Evaluation of machine learning techniques with AVIRIS-NG dataset in the identification and mapping of minerals.” *Advances in Space Research* 73, no. 2 (January 1, 2024): 1517–34. <https://doi.org/10.1016/j.asr.2022.09.018>.
- ALI, A., POUR, A. “Lithological mapping and hydrothermal alteration using Landsat 8 data: a case study in ariab mining district, red sea hills, Sudan.” *International Journal of Basic and Applied Sciences* 3, no. 3 (May 31, 2014). <https://doi.org/10.14419/ijbas.v3i3.2821>.
- BEA, F. “Uranium.” In *Encyclopedia of Geochemistry*, edited by C.P Marshall and Rhodes W. Fairbridge. Kluwer Academic Publishers, Dordrecht, 1999. <https://search.worldcat.org/title/956736090>.
- BILLINGS, S.D., FITZGERALD, D.J. “An integrated framework for interpolating airborne geophysical data with special reference to radiometrics.” *Exploration Geophysics (Melbourne, Vic. Online)/Exploration Geophysics* 29, no. 3–4 (September 1, 1998): 284–89. <https://doi.org/10.1071/eg998284>.
- BONHAM-CARTER, G. *Geographic Information systems for geoscientists*. Elsevier eBooks, 1994. <https://doi.org/10.1016/c2013-0-03864-9>.
- CAMPBELL, JAMES B., RANDOLPH H. WYNNE, AND VALERIE A. THOMAS. *Introduction to remote sensing*. 6th ed. Guilford Press, 2022.
- CASTELLA, M. “Unsupervised linear component analysis for a class of probability mixture models.” *IEEE Signal Processing Letters* 31 (January 1, 2024): 31–35. <https://doi.org/10.1109/lsp.2023.3341005>.
- CHAVEZ, P. S., GUPTILL, S. C., AND BOWELL, J. H. *Image processing techniques for thematic mapper data*. Technical Papers, Proceedings 50th Annual Meeting of ASPRS, Washington DC, U.S.A. Vol. 2. ASPRS, 1984.
- CUNEY, M. “Felsic magmatism and uranium deposits.” *Bulletin De La Société Géologique De France* 185, no. 2 (February 1, 2014): 75–92. <https://doi.org/10.2113/gssgfbull.185.2.75>.

- CUNEY, M., KYSER, K. “Chapter 2: Uranium Deposit Types and New Classifications” In *The Geology and Geochemistry of Uranium and Thorium Deposits*, 15–38. Mineralogical Association of Canada., 2016. <https://doi.org/10.3749/9780921294726.ch02>.
- DAHLKAMP, F.J “Argentina.” In *Uranium Deposits of the World, USA and Latin America.*, 427–45. Springer, Berlin, Heidelberg., 2010. https://doi.org/10.1007/978-3-540-78943-7_17.
- DAWOOD, Y.H., EL-NABY, H.H.A. “Genesis of uranyl mineralization in the Arabian Nubian Shield: A review.” *Journal of Asian Earth Sciences* 225 (March 1, 2022): 105047. <https://doi.org/10.1016/j.jseaes.2021.105047>.
- DE SOUZA GAIA, S.M., DE SOUZA FILHO, C.R. “Predictive mapping of prospectivity for gold in the central portion of the Tapajós Mineral Province, Brazil.” *Minerals* 13, no. 11 (November 12, 2023): 1432. <https://doi.org/10.3390/min13111432>.
- EL-RAOUF, A.A., DOĞRU, F., AZAB, I., JIANG, L., ABDELRAHMAN, K., FNAIS, M.S., AMER, O. “Utilizing Remote Sensing and Satellite-Based Bouguer Gravity data to Predict Potential Sites of Hydrothermal Minerals and Gold Deposits in Central Saudi Arabia.” *Minerals* 13, no. 8 (August 15, 2023): 1092. <https://doi.org/10.3390/min13081092>.
- EYAL, M., LITVINOVSKY, B., JAHN, B.M., ZANVILEVICH, A., KATZIR, Y. “Origin and evolution of post-collisional magmatism: Coeval Neoproterozoic calc-alkaline and alkaline suites of the Sinai Peninsula.” *Chemical Geology* 269, no. 3–4 (January 1, 2010): 153–79. <https://doi.org/10.1016/j.chemgeo.2009.09.010>.
- GAIKWAD, V., SINGH, K., SALUNKE, V., KUDNAR, N. “GIS-based comparative analysis of lineament extraction by using different azimuth angles: a case study of Mula river basin, Maharashtra, India.” *Arabian Journal of Geosciences* 16, no. 9 (August 31, 2023). <https://doi.org/10.1007/s12517-023-11636-2>.
- HAMIMI, Z., ELDOSOUKY, A.M., HAGAG, W., KAMH, S.Z. “Large-scale geological structures of the Egyptian Nubian Shield.” *Scientific Reports* 13, no. 1 (February 2, 2023). <https://doi.org/10.1038/s41598-023-29008-x>.
- IAEA. “Airborne gamma ray spectrometer surveying: Technical Reports Series No. 323.” Vienna, Austria: IAEA, Vienna, 1991. <https://www.iaea.org/publications/1427/airborne-gamma-ray-spectrometer-surveying>.
- IAEA. “Descriptive uranium deposit and mineral system models: Non-serial publications.” IAEA, Vienna, 2020. <https://www.iaea.org/publications/14663/descriptive-uranium-deposit-and-mineral-system-models>.
- IAEA. “Guidelines for radioelement mapping using Gamma Ray spectrometry data: IAEA-TECDOC-1363.” IAEA, Vienna, 2003. <https://www.iaea.org/publications/6746/guidelines-for-radioelement-mapping-using-gamma-ray-spectrometry-data>.
- IAEA. “Quantitative and spatial evaluations of undiscovered uranium resources: IAEA-TECDOC-1861.” IAEA, Vienna, 2018. <https://www.iaea.org/publications/12380/quantitative-and-spatial-evaluations-of-undiscovered-uranium-resources>.
- IAEA. “Uranium exploration data and techniques applied to the preparation of radioelement maps: IAEA-TECDOC-980.” IAEA, Vienna, 1997. <https://www.iaea.org/publications/5635/uranium-exploration-data-and-techniques-applied-to-the-preparation-of-radioelement-maps>.
- ISSA, R.A.M., AMARI, A.O.E., ALHANASH, H.B., ETMIMI, H.M. “Removal of uranium (VI) ion from aqueous solution using kaolinite.” *Kuwait Journal of Science* 50, no. 4 (October 1, 2023): 609–14. <https://doi.org/10.1016/j.kjs.2023.03.010>.

- JAVHAR, A., CHEN XI, J., AMINOV, J., MAMADJANOV, Y., AMINOV, J., DUULATOV, E., AND BAKHTIYOROV, Z. “Evaluation of remote sensing techniques for lithological mapping in the Southeastern Pamir using Landsat 8 OLI data.” *International Journal of Geoinformatics* 11, no. 1 (2018). <https://journals.sfu.ca/ijg/index.php/journal/article/view/1111>.
- KOVARCH, A., FLOOD, P.G., AND TYNE, E. Geographical Information Systems for Regional scale geological analysis: The Manilla 1: 250,000 Map Area, a case study. *Proceedings of the 7th Australian Remote Sensing Conference*, 1994.
- MAHDY, NASSER M., EL KALIOUBI, BAHER A., WOHLGEMUTH-UEBERWASSER, CORA C., SHALABY, MAHMOUD H., AND EL-AFANDY, ADEL H. “Petrogenesis of U- and Mo-bearing A2-type granite of the Gattar batholith in the Arabian Nubian Shield, Northeastern Desert, Egypt: Evidence for the favorability of host rocks for the origin of associated ore deposits.” *Ore Geology Reviews* 71 (December 1, 2015): 57–81. <https://doi.org/10.1016/j.oregeorev.2015.05.001>.
- MOUNTRAKIS, G., IM, J., OGOLE, C. Support vector machines in remote sensing: A review. *ISPRS Journal of Photogrammetry and Remote Sensing* 66 (2010), 247–259. <https://doi.org/10.1016/j.isprsjprs.2010.11.001>
- MOUSSA, E.M.M., STERN, R.J., MANTON, W.I., ALI, K.A. “SHRIMP zircon dating and Sm/Nd isotopic investigations of Neoproterozoic granitoids, Eastern Desert, Egypt.” *Precambrian Research* 160, no. 3–4 (February 1, 2008): 341–56. <https://doi.org/10.1016/j.precamres.2007.08.006>.
- OSMOND, J.K., DABOUS, A.A., DAWOOD, Y.H. “U series age and origin of two secondary uranium deposits, central Eastern Desert, Egypt.” *Economic Geology and the Bulletin of the Society of Economic Geologists* 94, no. 2 (April 1, 1999): 273–80. <https://doi.org/10.2113/gsecongeo.94.2.273>.
- PORWAL, A., DAS, R.D., CHAUDHARY, B., GONZALEZ-ALVAREZ, I., KREUZER, O. “Fuzzy inference systems for prospectivity modeling of mineral systems and a case-study for prospectivity mapping of surficial Uranium in Yeelirrie Area, Western Australia.” *Ore Geology Reviews* 71 (December 1, 2015): 839–52. <https://doi.org/10.1016/j.oregeorev.2014.10.016>.
- SABINS, F. F. “Remote sensing for mineral exploration.” *Ore Geology Reviews* 14, no. 3–4 (September 1, 1999): 157–83. [https://doi.org/10.1016/s0169-1368\(99\)00007-4](https://doi.org/10.1016/s0169-1368(99)00007-4).
- SHAWKY, M.M., EL-ARAFY, R.A., ZALAKY, M.A.E., ELARIF, T. “Integrated image processing and GIS-based techniques using knowledge-driven approaches to produce potential radioactivity map for the uraniumiferous granite of Egypt.” *NRIAG Journal of Astronomy and Geophysics* 8, no. 1 (January 2, 2019): 185–97. <https://doi.org/10.1080/20909977.2019.1667130>.
- SHEBL, A., ABRIHA, D., FAHIL, A.S., EL-DOKOUNY, H.A., ELRASHEED, A.A., CSÁMER, Á. “PRISMA hyperspectral data for lithological mapping in the Egyptian Eastern Desert: Evaluating the support vector machine, random forest, and XG boost machine learning algorithms”. *Ore Geology Reviews* 161 (2023), 105652. <https://doi.org/10.1016/j.oregeorev.2023.105652>
- SHUIBO, X., CHUN, Z., XINGHUO, Z., JING, Y., XIAOJIAN, Z., JINGSONG, W. “Removal of uranium (VI) from aqueous solution by adsorption of hematite.” *Journal of Environmental Radioactivity* 100, no. 2 (February 1, 2009): 162–66. <https://doi.org/10.1016/j.jenvrad.2008.09.008>.

- VERMILLION, S. C., AND SADER, S. A. Use of the minimum noise Fraction (MNF) transform to analyze airborne Visible/infrared Imaging Spectrometer (AVIRIS) data of northern forest types. AVIRIS Proceedings (JPL Publication 99-17). NASA, 1999.
https://aviris.jpl.nasa.gov/proceedings/workshops/99_docs/62.pdf.
- WAHEEB, A. “Determination of Tectonic Regimes at Gabal Abu Harba Granites and Their Relation to the Distribution of Secondary Uranium Minerals, Northern Eastern Desert, Egypt.” Egyptian Journal of Geology 60 (2016): 212–30.

Author:

¹ Islam Azab - Nuclear Materials Authority, Egypt, P.O. Box 530 El-Maadi, Cairo, islam_nma2010@yahoo.com